Japanese Journal of
Applied Physics

PROGRESS REVIEW

Magnetic sensing and imaging using nanodiamond NV center films and microwave integration into an STM coplanar waveguide stage

To cite this article: Toyo Kazu Yamada *et al* 2026 *Jpn. J. Appl. Phys.* **65** 050803

Japanese Journal of Applied Physics **65**, 050803 (2026)
https://doi.org/10.35848/1347-4065/ae4a30

PROGRESS REVIEW

Magnetic sensing and imaging using nanodiamond NV center films and microwave integration into an STM coplanar waveguide stage

Toyo Kazu Yamada[1,2*], Achmad Yahiya Koki[1], and Mai Niida[1]

[1]*Department of Materials Science, Chiba University, 1-33 Yayoi-Cho, Inage-Ku, Chiba 263-8522, Japan*
[2]*Molecular Chirality Research Centre, Chiba University, 1-33 Yayoi-cho, Inage-Ku, Chiba 263-8522, Japan*

*E-mail: toyoyamada@faculty.chiba-u.jp

Received January 15, 2026; revised February 19, 2026; accepted February 24, 2026; published online March 16, 2026

Spin-polarized scanning tunneling microscopy (SP-STM) enables access to the spin polarization of individual magnetic atoms but is inherently insensitive to magnetic fields. In contrast, nitrogen-vacancy (NV) centers in diamond provide highly sensitive magnetic-field detection through optically detected magnetic resonance (ODMR). Integrating ODMR-based magnetic-field sensing with SP-STM therefore offers a pathway to comprehensive magnetic characterization from the atomic scale to long-range fields. Here, we demonstrate that drop-cast nanodiamond (ND) films with an average particle size of ~100 nm deposited on glass substrates function as magnetic-field sensors for imaging magnetic domains under ambient conditions using a conventional ODMR setup. The random orientations of NV centers in the ND ensemble enable detection of magnetic fields with arbitrary directions without crystallographic alignment. Furthermore, we report progress toward integrating ODMR with SP-STM by developing an STM stage equipped with a coplanar waveguide, enabling reliable microwave delivery to the STM junction.

1. Introduction

Magnetic imaging techniques operable at room temperature (300 K) have been extensively developed over the past two decades. Representative methods include spin-polarized scanning tunneling microscopy (SP-STM),[1–3] which detects spin polarization vectors proportional to the local atomic spin angular momentum with atomic-scale resolution; magnetic force microscopy,[4–6] which measures magnetic forces from ferromagnetic samples with a typical spatial resolution of 10–50 nm; and scanning electron microscopy with polarization analysis,[7,8] which detects asymmetries in spin-polarized secondary electrons with a spatial resolution of approximately 10–100 nm.

Among these techniques, nitrogen-vacancy (NV) centers in diamond have attracted considerable attention as a promising platform for magnetic imaging because of their high sensitivity to local magnetic fields.[9–12] In particular, the recent commercial availability of nanodiamonds (NDs) attached to cantilever tips[13,14] or single-crystal diamond cantilevers[15] has enabled the detection of magnetic fields from nanoscale magnetic structures. However, while typical NDs have diameters in the range of 50–200 nm, smaller NDs (<10 nm) tend to host less stable NV centers, leading to reduced sensitivity. Consequently, ND-based magnetic sensors are currently more suitable for applications such as magnetic sensing of biological materials in liquid environments[16,17] rather than for high-resolution magnetic imaging.[18,19] Owing to the finite size of NDs, the achievable magnetic spatial resolution is generally limited to micrometer scales, and atomic-scale magnetic imaging, as achieved by SP-STM, remains inaccessible.

Magnetic resonance of NV centers in diamond using a visible laser can be measured as follows.[20,21] The negatively charged NV^- center possesses a spin-triplet ($S = 1$) ground state, which is split into the $|m_s = 0\rangle$ and $|m_s = \pm 1\rangle$ sublevels by a zero-field splitting of approximately 2.87 GHz, even in the absence of an external magnetic field. Optical excitation with green light ($\lambda = 532$ nm) promotes electrons from the ground state to the excited state, followed by radiative relaxation that produces red photoluminescence centered at $\lambda = 637$ nm. When magnetic resonance occurs between the ground-state spin sublevels, the probability of nonradiative decay via intermediate singlet states increases. This spin-dependent intersystem crossing alters the population distribution between the $M_s = \pm 1$ and $M_s = 0$ states, resulting in spin polarization and a reduction in the photoluminescence intensity. This change enables the detection of magnetic resonance through optical means, a technique known as optically detected magnetic resonance (ODMR).

In this progress review, we present a simple and versatile magnetic imaging method based on ND films drop-cast onto glass substrates and positioned at the focal plane of an optical microscope [Fig. 1(a)]. Using ODMR, this configuration enables the visualization of magnetic patterns with micrometer-scale spatial resolution under ambient conditions. The ND films contain a high density of NV centers with randomly oriented spin axes, allowing detection of magnetic fields with arbitrary directions. As a result, the obtained CMOS images reflect variations in the local magnetic field amplitude rather than vectorial field information.

Furthermore, we extend this ND-based ODMR approach by integrating it with SP-STM operated under ultrahigh-vacuum conditions. To achieve this, we developed a modified STM sample stage incorporating a coplanar waveguide (CPW) design. The STM sample holder was engineered to allow repeated insertion and removal from the STM stage while maintaining efficient microwave delivery. After several design iterations, we successfully achieved microwave transmission efficiencies exceeding 90% to the STM stage by employing compact permanent magnets, nickel foils, and a CPW integrated directly into the STM sample holder.

Thus, combining SP-STM with ND-based ODMR enables comprehensive magnetic imaging spanning length scales from the atomic to the micrometer regime.

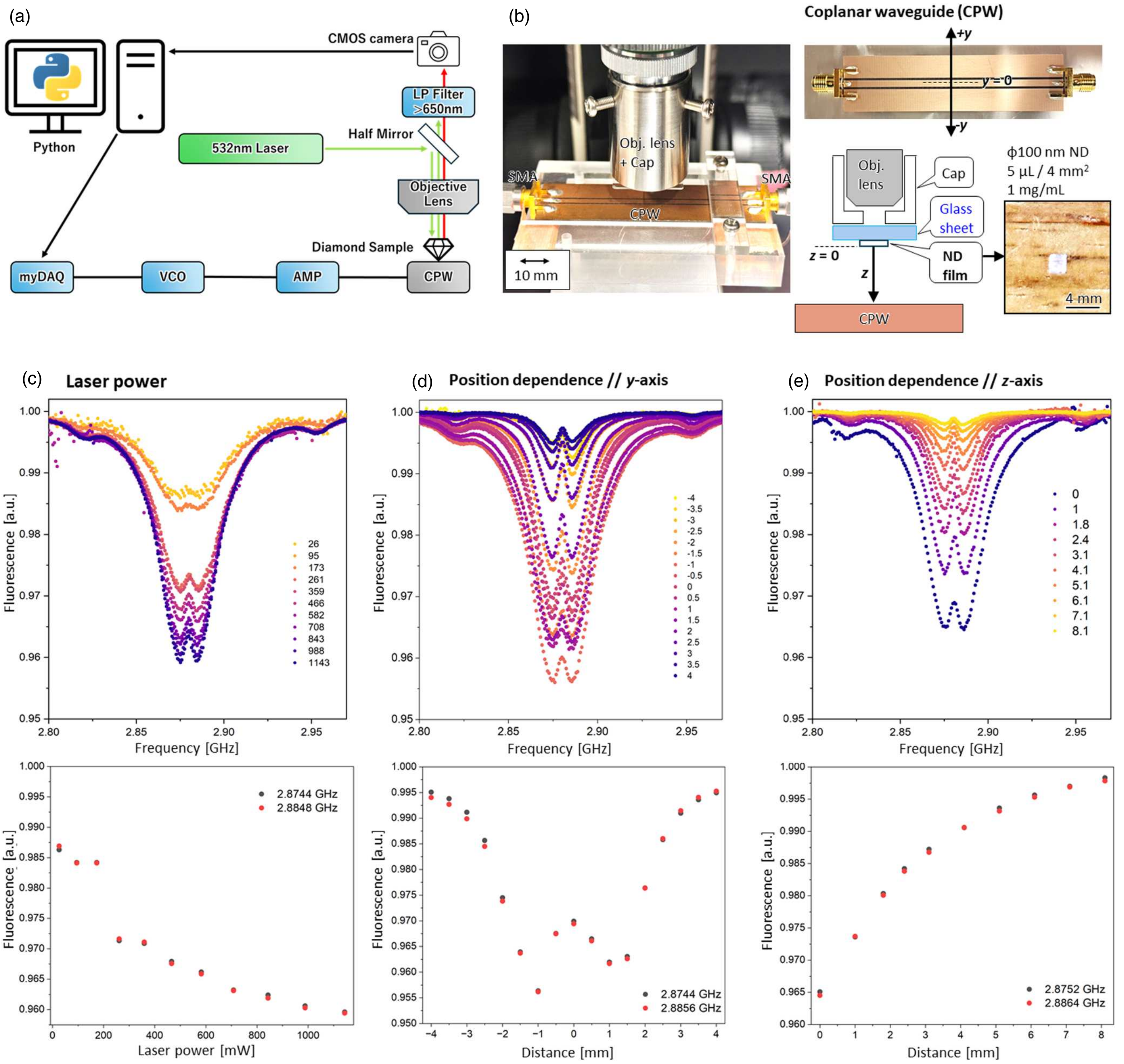

Fig. 1. ODMR measurements using nanodiamond (ND) films containing NV centers. (a) Schematic diagram of the ODMR measurement setup. (b) Photograph of the home-built ODMR system. The objective lens is capped to fix the ND-film-coated glass plate at the focal position, and a typical coplanar waveguide (CPW) is employed. The definitions of the *y* and *z* axes are indicated. (c) ODMR spectra acquired at different excitation laser powers. The lower panel shows the fluorescence intensities measured at 2.8744 GHz (black dots) and 2.8848 GHz (red dots) as a function of the incident laser power. (d) ODMR spectra measured at different positions along the *y* axis. The lower panel shows the fluorescence intensities measured at 2.8744 GHz (black dots) and 2.8856 GHz (red dots) as a function of the *y* position. (e) ODMR spectra measured at different positions along the *z* axis, where $z = 0$ corresponds to the contact between the CPW and the ND film. The lower panel shows the fluorescence intensities measured at 2.8752 GHz (black dots) and 2.8864 GHz (red dots) as functions of the *z* position.

2. Progress in experimental studies

2.1. ODMR setup

Figure 1(a) shows a schematic diagram of the experimental ODMR setup. A typical optical microscope was used for optical measurements. A 532 nm continuous-wave laser served as the excitation light source. The laser beam was reflected by a half mirror inside the microscope and focused onto the diamond sample through an objective lens with a numerical aperture of 0.4. Using the same optical path, the emitted photoluminescence from the diamond passed back through the objective lens and the half mirror, after which a long-pass filter blocked light with wavelengths shorter than 650 nm. Only the red photoluminescence was detected by a CMOS camera (Basler ace acA720-520um), and the images were recorded using a personal computer. To compensate for fluctuations in laser intensity, the photoluminescence intensity measured with microwave irradiation was normalized by that measured without microwave irradiation at each frequency point to obtain the ODMR spectra.

Simultaneously with the optical excitation, microwaves were applied to the diamond sample. The microwave frequency was controlled by a Python program on the PC via a data acquisition device (myDAQ, National Instruments), which supplied a voltage signal to a voltage-controlled oscillator (Mini-Circuits) operating in the frequency range of 2.7–3.1 GHz. A microwave power of 10 dBm, corresponding to 10 mW, was applied. The microwave signal was subsequently amplified and delivered to a home-built CPW fabricated from a commercial copper-coated printed circuit board (PCB). The diamond sample was placed directly on the CPW.

Figure 1(b) shows a photograph of the experimental setup. For magnetic sensing, a cap was mounted to cover the objective lens, with a central aperture allowing the optical beam to pass through. A glass plate coated with ND films was placed on top of the cap at the focal plane of the objective lens. In the CPW photograph, the y-axis is defined such that $y = 0$ corresponds to the center of the CPW. The central copper strip serves as the microwave transmission path between the SMA connectors. In the corresponding cross-sectional schematic, the z-axis is defined, with $z = 0$ corresponding to the position where the ND film surface is in contact with the sample. The right-lower panel of Fig. 1(b) shows a photograph of ND films deposited on the glass plate. The films were prepared by drop-casting a carboxylated ND solution with an average particle diameter of approximately 100 nm and a concentration of 1 mg ml^{-1} (Adamas Nanotechnologies). Given an NV center concentration of ~3 ppm, each ND contains approximately 300 NV centers. A 5 μl droplet was deposited over an area of 2 × 2 mm^2 and dried in air, forming a white, box-shaped film.

2.2. Spatial variation of ODMR spectra relative to the CPW

Figure 1(c) shows representative ODMR spectra, fluorescence intensity (arb. units: a.u.) is plotted as a function of the microwave (GHz). The upper panel displays two symmetric dip features centered around 2.874 and 2.885 GHz, corresponding to the NV$^-$ spin transitions. In our setup, the observed ODMR contrast depends on the excitation laser power. The lower panel shows the fluorescence intensities around 2.8744 GHz (black dots) and 2.8848 GHz (red dots), measured at the dip positions, as a function of the incident laser power. In our setup, to acquire wide-area magnetic images, the distance between the objective lens and the ND may be slightly defocused. Therefore, a relatively high initial laser power is required to obtain clear ODMR signals. Also, the laser and microwave are introduced at the same time (CW-ODMR), where the polarization is in a nonequilibrium steady state, and it requires higher laser power to have larger polarization to show high ODMR contrast [Fig. 1(c)].

Figure 1(d) shows ODMR spectra acquired by laterally shifting the ND film across the CPW along the y-axis, while the lower panel displays fluorescence intensities at the dip positions along the y-axis. The results indicate that the microwave field extends more than 3 mm from the center of the CPW. Two dips are observed near the signal lines at $y \approx \pm 1$ mm, close to the strip edges of the CPW surface, indicating that the microwave field preferentially spreads from the edges.

It is also important to evaluate the decay of the microwave field along the z-axis, since magnetic samples are placed on the CPW surface and may be separated from it by a finite distance. Figure 1(e) shows the z dependence of the ODMR signal intensity. The fluorescence intensities of the two dips gradually decay with increasing distance, as more clearly visible in the lower panel. These results indicate that the microwave field extends up to approximately 8 mm from the CPW surface. For magnetic measurements, a magnet thickness of 0–2 mm is therefore suitable for effective microwave application.

2.3. Nanodiamond-based magnetic sensing and imaging

The detectability of the ODMR signal primarily arises from spin-state polarization induced by laser illumination, while the functionality as a qubit also critically depends on how effectively the quantum spins are electronically decoupled from the surrounding conduction electrons. Electron transport in typical electronic environments can induce spin flips via inelastic scattering, thereby shortening the qubit lifetime. NV centers constitute one of the few experimentally realized solid-state qubits that can operate at room temperature (300 K) under ambient conditions.

Owing to their high sensitivity to external magnetic fields, NV centers are particularly well suited for detecting stray magnetic fields and can function as highly sensitive magnetic sensors. To investigate the continuous magnetic-field dependence of the ODMR signal, external magnetic fields were applied to the ND film placed on the CPW. Home-built Helmholtz coils were used to generate an in-plane magnetic field along the x-axis, while an electromagnet was employed to apply an out-of-plane magnetic field along the z-axis.

Figures 2(a) and 2(b) show the ODMR spectra obtained under in-plane (x-axis) and out-of-plane (z-axis) magnetic fields, respectively. During these measurements, the positions of the ND film and the CPW were fixed at $y = 0$ mm and $z = 0$ mm. The ODMR spectra vary continuously with the applied magnetic field. For the in-plane magnetic field, fields in the range of 0–2 mT were applied [left panel of Fig. 2(a)]. In this configuration, the two ODMR dips varied with an application of approximately 0.1 mT within an averaging time of 50 ms. In contrast to the behavior observed for single-crystal diamond, NDs exhibit a continuous change in the dip intensity accompanied by shifts of the peak tails toward both lower and higher frequencies, consistent with previous reports.[21] These variations are more clearly visualized in the two-dimensional (2D) ODMR map shown in the right panel of Fig. 2(a), which highlights the evolution of the ODMR dips as a function of the applied magnetic field. The frequency-dependent shift of the dip tails was fitted with a quadratic function [white lines in the right panel of Fig. 2(a)], suggesting potential applicability for magnetic-field sensing. We also examined how the fluorescence intensity at the dip position (2.8704 GHz) and the intensity measured near the dip, where a sharp intensity variation is observed (2.8640 GHz), depend on the in-plane magnetic field, as shown in the lower panel of Fig. 2(a). We initially expected a linear dependence on the magnetic field; however, the spectra exhibit distinct fluorescence intensity behaviors. Specifically, the intensity at the dip position shows little change in the range of 0.0–0.4 mT (black dots) and begins to increase linearly above 0.5 mT. In contrast, the intensity at 2.8640 GHz decreases with increasing magnetic field up to 0.7 mT and then increases linearly at higher fields (see red dots and the fitted curve), similar to the behavior at the dip position.

Figure 2(b) shows ODMR spectra acquired under an out-of-plane magnetic field applied along the z direction ($B = 0$–

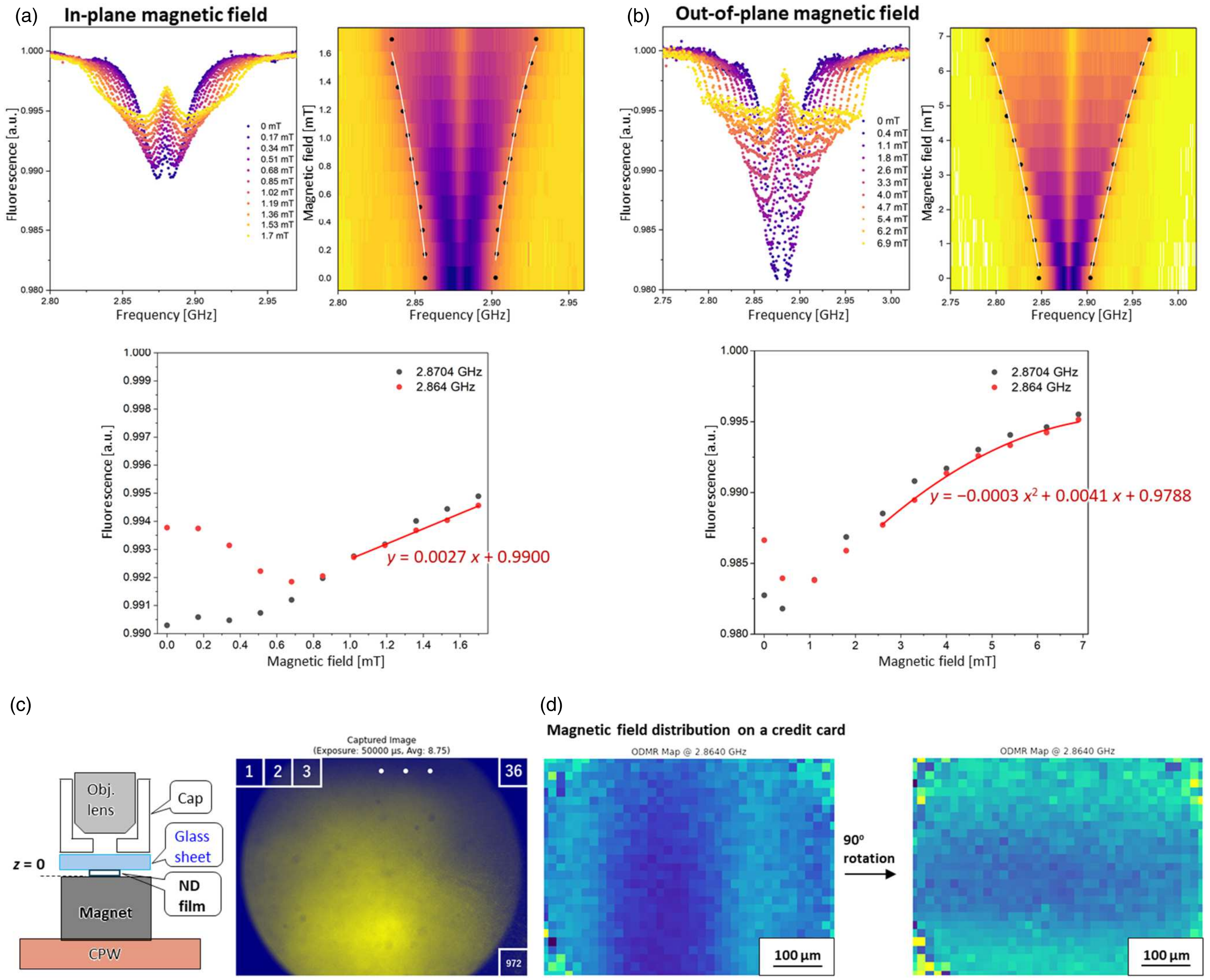

Fig. 2. Magnetic field dependence of ODMR and magnetic imaging using ND films containing NV centers. (a), (b) The left panels: ODMR spectra acquired under different applied magnetic fields in the (a) in-plane and (b) out-of-plane directions. The right panels: 2D ODMR maps as a function of microwave frequency and magnetic field. The white lines represent quadratic fits. The lower panels display fluorescence intensities measured at ~2.87 GHz (black dots) and ~2.86 GHz (red dots) as a function of the applied magnetic field. (c) ODMR setup for magnetic imaging, where the surface of the magnet is in contact with the ND film. The right panel shows a CMOS camera image consisting of 720 × 540 pixels; the data were averaged into 36 × 27 blocks to generate the magnetic image. (d) CMOS camera images in the *x*–*y* plane acquired at 2.864 GHz, showing pronounced variations induced by the magnetic fields originating from the credit card surface. The right panel was obtained after rotating the sample by 90°.

7 mT). Again, the two ODMR dips are sensitive to the magnetic field and exhibit continuous changes in dip intensity with increasing field strength. In addition, the dip tails broaden with increasing magnetic field, as clearly seen in the corresponding 2D ODMR map [right panel of Fig. 2(b)]. Fitting these variations with a quadratic function indicates that they depend continuously on the applied field.

The lower panel of Fig. 2(b) shows the fluorescence intensities at the dip position (2.8704 GHz, black dots) and at a frequency close to the dip, where the intensity changes drastically with the applied magnetic field (2.8640 GHz, red dots), as functions of the out-of-plane magnetic field. As in the case of an in-plane magnetic field, the fluorescence intensities measured at approximately 2.8704 and 2.8640 GHz decrease for magnetic fields below 1 mT, but increase with increasing out-of-plane magnetic field above 1 mT, following a quadratic dependence (see the red data points and the fitted curve).

It should be noted that the difference in ODMR contrast between Figs. 2(a) and 2(b) arises from slight variations in defocusing and ND positioning, as the setup had to be reconfigured for in-plane and out-of-plane magnetic field applications.

Following these magnetic sensing experiments using NDs, we next demonstrate their applicability to magnetic imaging of samples that generate stray magnetic fields at the surface. By spatially mapping the stray magnetic field with a CMOS camera, magnetic imaging is achieved by detecting photoluminescence intensity variations at each pixel at a selected microwave frequency. In this demonstration, we used an objective lens with a magnification of 20×, yielding a CMOS image size of 590 μm × 440 μm. A credit card, which produces an out-of-plane surface stray field of approximately ~0.09 mT as measured by a Hall probe, was used as the sample.

Figure 2(c) shows a representative example of the imaging procedure. A single camera image consisting of 720 × 540 pixels was recorded with an exposure time of 50 ms. To improve the signal-to-noise ratio, the image was divided into 36 × 27 blocks, with each block corresponding to the average signal from 20 × 20 pixels. The right panel of Fig. 2(c) shows an example CMOS camera image, which is divided into separate blocks. The microwave frequency was set near 2.86 GHz, where pronounced ODMR signal variations were observed in Figs. 2(a) and 2(b).

Figure 2(d) shows a 2D ODMR map in the *x*–*y* plane measured at 2.8640 GHz, corresponding to magnetic imaging of a credit card and revealing micrometer-scale magnetic domains. Stripe-like patterns are clearly visible in the ODMR maps, and their orientation rotates in accordance with the rotation of the credit card. This behavior confirms that the NV spins detect stray magnetic fields originating from the magnetic domains of the card.

2.4. ODMR measurements on the STM–CPW stage

As our ultimate goal is to integrate ODMR-based magnetic imaging with SP-STM, it is necessary to implement a CPW on the UHV-STM sample stage. Figure 3(a) summarizes the experimental configurations investigated in this study. Our initial approach involved a direct miniaturization of a conventional CPW design. As shown in Fig. 1(c), the standard CPW (dimensions: 70 mm × 19 mm) consists of a PCB substrate with a thickness of 1.6 mm, with both surfaces coated with copper foil of 0.018 mm thickness. Two channels were fabricated by selectively removing the copper foil, such that the microwave signal propagates along the central copper trace while the two side copper planes are grounded through electrical contact with SMA connectors.

To evaluate microwave transmission through the CPW, both SMA terminals were connected to a vector network analyzer (VNA), and the reflection coefficient $|S_{11}|$ was measured in the frequency range of 2–3 GHz, as shown in Fig. 3(c). The response of the standard CPW is shown by the black curve, indicating that approximately 10%–40% of the incident microwave power was transmitted, while the reflection coefficient exhibited pronounced frequency-dependent oscillations.

For integration into the STM, the CPW had to be miniaturized to match the dimensions of the STM sample stage (15 mm × 15 mm). A CPW of this size was fabricated

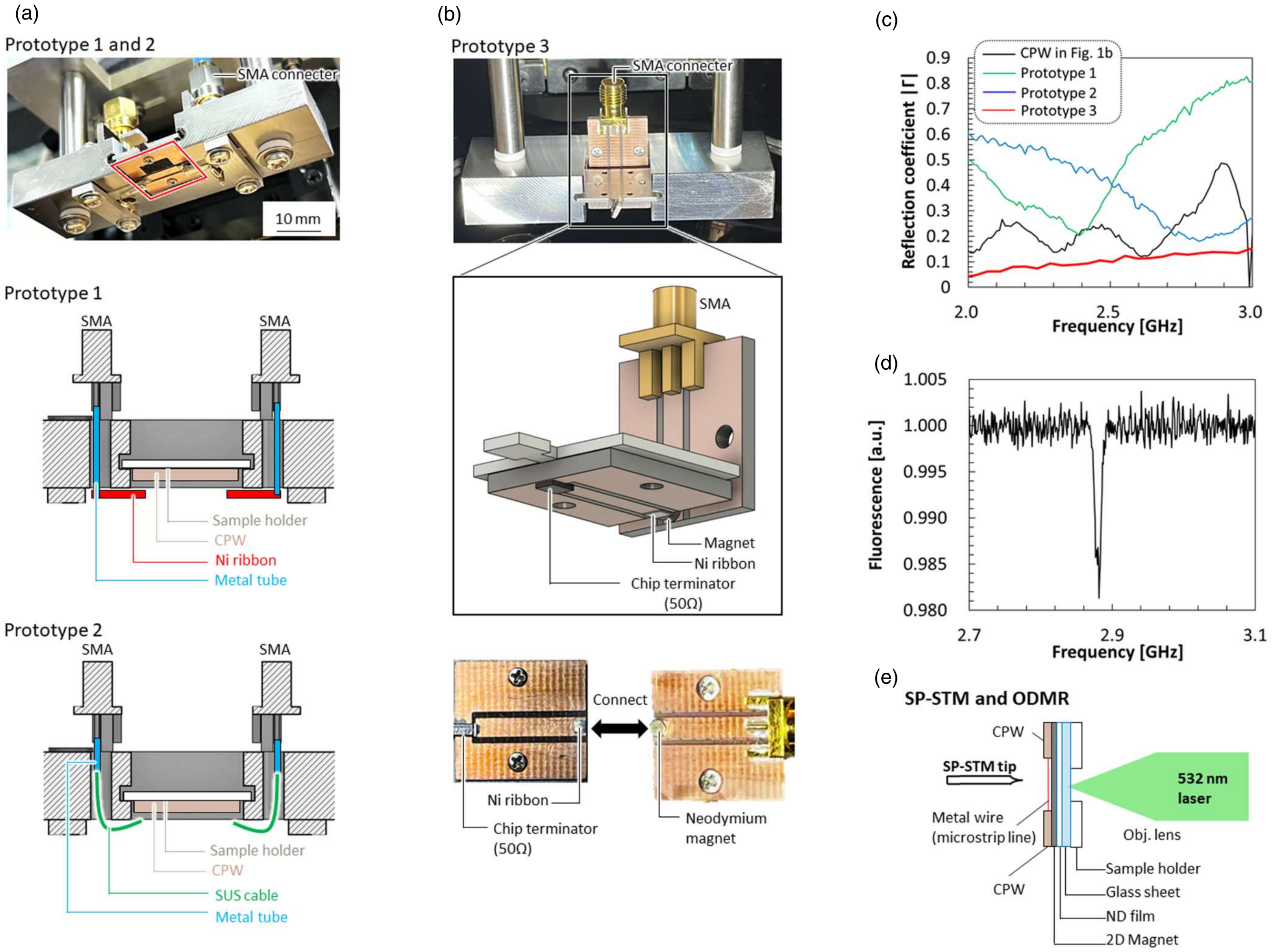

Fig. 3. Development of CPW stages for introducing microwaves into a STM. (a), (b) Photographs and CAD cross-sectional views of (a) prototypes 1 and 2 and (b) prototype 3 setups. The STM stage and STM sample plate are electrically connected using Ni ribbons and neodymium magnets, while the microwave path is terminated at the sample stage with a 50 Ω load. (c) Reflection coefficients measured using a vector network analyzer (VNA). The black curve corresponds to the standard PCB-CPW shown in Fig. 1(b). The blue and green curves were obtained from the prototype 1 setup using a metal tube with a Ni ribbon and the prototype 2 setup using a metal tube with a stainless-steel (SUS) cable, respectively. The red curve was measured from the prototype 3 setup. In the frequency range of 2–3 GHz, more than 90% of the microwave signal is transmitted. (d) ODMR spectrum obtained using the prototype 3 setup with the diamond NV centers. (e) Current experimental setup under development for combined SP-STM and ODMR measurements in UHV.

with the same channel structure. A further challenge arises from the requirement that the STM sample stage be repeatedly mounted and unmounted, which precludes direct electrical contact between the SMA connector and the STM CPW plate. Consequently, the SMA connectors and the STM stage must be mechanically separated, necessitating an alternative method for microwave transmission with minimal loss.

To address this issue, we employed a weak attractive contact formed between a 2 mm wide nickel (Ni) ribbon foil and a 2 mm sized neodymium magnet. Although NV centers are sensitive to magnetic fields, the ND film sample is located at the center of the STM stage, while the magnet is positioned more than 5 mm away from the diamond. Furthermore, the magnetic field strength of the magnet was reduced from 2.4 mT to 0.7 mT by annealing it in air at 523 K for 5 min; the resulting stray field was measured using a Hall probe positioned 5 mm from the magnet surface.

In the first prototype [prototype 1 in Fig. 3(a)], metallic tubes were inserted into the SMA terminals and bonded to Ni ribbon foils, which were then brought into contact with the neodymium magnet to transfer the microwave signal into the STM CPW stage. However, VNA measurements revealed that 20%–80% of the incident power was reflected, as indicated by the green curve in Fig. 3(c). In a subsequent attempt [prototype 2 in Fig. 3(a)], the Ni ribbon foils were replaced with stainless steel coaxial cables (Cooner Wire, 50 pF m^{-1}), which are commonly used for STM tunneling current measurements. Nevertheless, significant reflections persisted, with 20%–60% of the power reflected [blue curve in Fig. 3(c)]. Based on these results, we concluded that the use of two SMA terminals was unsuitable for efficient microwave coupling.

Thus, we developed an improved configuration [prototype 3 in Fig. 3(b)], in which the CPW was equipped with a single SMA connector, while the opposite end was terminated with a 50 Ω load connected to ground. As shown by the red curve in Fig. 3(c), this design enabled highly efficient microwave transmission: more than 90% of the incident microwave power was successfully coupled into the STM CPW stage across the entire frequency range of 2–3 GHz. This configuration establishes reliable electrical contact between the nickel ribbon and the 2 mm sized neodymium magnet and provides stable, low-loss microwave delivery to the STM stage.

Figure 3(d) demonstrates ODMR spectra obtained from a bulk NV diamond crystal (Element Six, MONODITE MCC, Single Crystal CVD—Colorless) placed on the STM CPW stage, confirming the successful detection of ODMR signals under STM-compatible conditions.

Finally, Fig. 3(e) illustrates our current experimental setup integrating SP-STM with ODMR. In this configuration, NDs are used as spin sensors for magnetic metal samples and molecular spin systems. Because this approach requires an atomically flat surface, we fabricated a CPW on a Cu film/PCB substrate with a central aperture (alternatively, a transparent glass or sapphire substrate can be used), onto which the NDs are deposited. A conductive 2D material, such as a 2D magnet[22] or graphene,[23,24] is then placed on top of the ND layer. This overlayer provides a conductive pathway for the tunneling current between the STM tip and the sample while preserving atomic-scale flatness. By integrating these components, our setup enables simultaneous detection of spin information using both SP-STM and ODMR.

3. Conclusions

In summary, we have demonstrated that ND films deposited on a glass substrate can function as magnetic imaging sensors based on ODMR. The ND films were prepared by drop-casting a 5 μl droplet of a carboxylated ND solution (average diameter ~100 nm; concentration 1 mg ml^{-1}) onto a box-shaped area of 2×2 mm^2 and drying in air. The resulting ODMR spectra exhibit continuous and systematic shifts in response to applied magnetic fields, enabling quantitative magnetic-field detection and imaging. Furthermore, we successfully designed the STM CPW stage. After overcoming several technical challenges related to microwave transmission, we achieved efficient coupling of more than 90% of the microwave power into the STM stage. As a result, sharp and well-defined ODMR signals were obtained from the NV centers within diamond placed on the STM CPW. These results indicate the feasibility of combining ODMR-based magnetic imaging with SP-STM, opening a pathway toward correlative magnetic measurements with both high spatial resolution and quantum spin sensitivity.

Acknowledgments

This work was supported by JSPS KAKENHI Grant No. 23H02033. We are grateful to Dr. Kento Sasaki, Dr. Kensuke Kobayashi, Dr. Masahiro Haze (The University of Tokyo), and Dr. Hitoshi Ishiwata (QST) for their valuable discussions and technical assistance. We express our appreciation to Mr. Haruto Shibahara for constructing the Helmholtz coil setup. We thank Dr. Eiichi Inami (Kochi University of Technology) for carefully reviewing the manuscript and for providing valuable suggestions for its improvement.

Conflicts of interest

The authors declare no competing financial interest.

ORCID iDs

Toyo Kazu Yamada https://orcid.org/0000-0001-5185-6472

---

1) U. Schlickum, N. Janke-Gilman, W. Wulfhekel, and J. Kirschner, "Step-induced frustration of antiferromagnetic order in Mn on Fe(001)," Phys. Rev. Lett. **92**, 107203 (2004).
2) T. K. Yamada, M. M. J. Bischoff, G. M. M. Heijnen, T. Mizoguchi, and H. van Kempen, "Observation of spin-polarized surface states on ultrathin Bct Mn(001) films by spin-polarized scanning tunneling spectroscopy," Phys. Rev. Lett. **90**, 056803 (2003).
3) T. K. Yamada, M. M. J. Bischoff, G. M. M. Heijnen, T. Mizoguchi, and H. Van Kempen, "Origin of magnetic contrast in spin-polarized scanning tunneling spectroscopy: experiments on ultra-thin Mn films," Jpn. J. Appl. Phys. **42**, 4688 (2003).
4) X. Zhu, P. Grütter, V. Metlushko, and B. Ilic, "Magnetic force microscopy study of electron-beam-patterned soft permalloy particles: technique and magnetization behavior," Phys. Rev. B **66**, 024423 (2002).
5) T. Okuno, K. Shigeto, T. Ono, K. Mibu, and T. Shinjo, "MFM study of magnetic Vortex cores in circular permalloy dots: behavior in external field," J. Magn. Magn. Mater. **240**, 1 (2002).

6) M. V. Makarova, Y. Akaishi, Y. Suzuki, K. S. Rao, S. Yoshimura, and H. Saito, "High-resolution alternating magnetic force microscopy using an amorphous FeB-Based tip driven by an inverse magnetostrictive effect: imaging of the high-density magnetic recording media," J. Magn. Magn. Mater. **546**, 168755 (2022).
7) J. Unguris, R. J. Celotta, D. A. Tulchinsky, and D. T. Pierce, "Exchange coupling in magnetic multilayers grown on iron whiskers," J. Magn. Magn. Mater. **198–199**, 396 (1999).
8) D. T. Pierce, J. Unguris, R. J. Celotta, and M. D. E. Stiles, "!Ect of roughness, frustration, and antiferromagnetic order on magnetic coupling of Fe/Cr multilayers," J. Magn. Magn. Mater. (1999).
9) J. Wrachtrup, C. Von Borczyskowski, J. Bernard, M. Orrit, and R. Brown, "Optical detection of magnetic resonance in a single molecule," Nature **363**, 244 (1993).
10) J. F. Barry, J. M. Schloss, E. Bauch, M. J. Turner, C. A. Hart, L. M. Pham, and R. L. Walsworth, "Sensitivity optimization for NV-diamond magnetometry," Rev. Mod. Phys. **92**, 015004 (2020).
11) S. Hong, M. S. Grinolds, L. M. Pham, D. Le Sage, L. Luan, R. L. Walsworth, and A. Yacoby, "Nanoscale magnetometry with NV centers in diamond," MRS Bull. **38**, 155 (2013).
12) C. Zhang et al., "Optimizing NV magnetometry for magnetoneurography and magnetomyography applications," Front. Neurosci. **16**, 1034391 (2023).
13) B. K. Dadhich, B. Panda, M. S. Sidhu, and K. P. Singh, "Nanodiamonds enable femtosecond-processed ultrathin glass as a hybrid quantum sensor," Sci. Rep. **13**, 6286 (2023).
14) Y. Gokhale et al., "Self-aligned multilayered nitrogen vacancy diamond nanoparticles for high spatial resolution magnetometry of microelectronic currents," Nano Lett. **25**, 9204 (2025).
15) D. Rohner, J. Happacher, P. Reiser, M. A. Tschudin, A. Tallaire, J. Achard, B. J. Shields, and P. Maletinsky, "(111)-Oriented, single crystal diamond tips for nanoscale scanning probe imaging of out-of-plane magnetic fields," Appl. Phys. Lett. **115**, 192401 (2019).
16) M. Fujiwara, A. Dohms, K. Suto, Y. Nishimura, K. Oshimi, Y. Teki, K. Cai, O. Benson, and Y. Shikano, "Real-time estimation of the optically detected magnetic resonance shift in diamond quantum thermometry toward biological applications," Phys. Rev. Res. **2**, 043415 (2020).
17) Y. Nishimura et al., "Wide-field fluorescent nanodiamond spin measurements toward real-time large-area intracellular thermometry," Sci. Rep. **11**, 4248 (2021).
18) Y.-A. Du, Q. Ying, C. Li, S.-C. Zhang, F.-W. Sun, A. Du, H. Qin, and Y. Pan, "Scanning magnetic imaging of geological samples based on fiber-coupled diamond quantum magnetometry," Phys. Rev. Appl. **24**, 034036 (2025).
19) R. Kitagawa, T. Kohashi, T. Tsuji, S. Nagata, A. Nakatsuka, H. Nitta, Y. Takamura, S. Nakagawa, T. Iwasaki, and M. Hatano, "Wide-field imaging of the magnetization process in soft magnetic-thin film using diamond quantum sensors," Appl. Phys. Express **17**, 017002 (2024).
20) Y. Doi et al., "Deterministic electrical charge-state initialization of single nitrogen-vacancy center in diamond," Phys. Rev. X **4**, 011057 (2014).
21) M. Tsukamoto, S. Ito, K. Ogawa, Y. Ashida, K. Sasaki, and K. Kobayashi, "Accurate magnetic field imaging using nanodiamond quantum sensors enhanced by machine learning," Sci. Rep. **12**, 13942 (2022).
22) A.-A. Haghighirad et al., "STM imaging and electronic correlation in van der waals ferromagnet Fe_3 $GeTe_2$," Jpn. J. Appl. Phys. **64**, 040805 (2025).
23) C. G. Ayani, F. Calleja, I. M. Ibarburu, P. Casado Aguilar, N. K. M. Nazriq, T. K. Yamada, M. Garnica, A. L. Vázquez De Parga, and R. Miranda, "Switchable molecular functionalization of an STM Tip: from a Yu–Shiba–Rusinov Tip to a Kondo Tip," Nanoscale **14**, 15111 (2022).
24) T. K. Yamada, H. Fukuda, T. Fujiwara, P. Liu, K. Nakamura, S. Kasai, A. L. Vazquez de Parga, and H. Tanaka, "Energy gap opening by crossing drop cast single-layer graphene nanoribbons," Nanotechnology **29**, 315705 (2018).